Article:
Dodd, M, Shi, W, Li, C et al. (Cover date: 29 June 2023) Uncovering the Ediacaran phosphorus cycle. Nature, 618. pp. 974-980. ISSN: 0028-0836

https://doi.org/10.1038/s41586-023-06077-6

Uncovering the Ediacaran phosphorus cycle

Matthew S. Dodd[a,b,c], Wei Shi[a,c], Chao Li[a,b,c*], Zihu Zhang[a,c], Meng Cheng[a,c], Haodong Gu[b], Dalton S. Hardisty[d], Sean J. Loyd[e], Malcolm W. Wallace[f], Ashleigh vS. Hood[f], Kelsey Lamothe[f], Benjamin J. W. Mills[g], Simon W. Poulton[g], Timothy W. Lyons[h]

[a] State Key Laboratory of Oil and Gas Reservoir Geology and Exploitation & Institute of Sedimentary Geology, Chengdu University of Technology, Chengdu 610059, China
[b] State Key Laboratory of Biogeology and Environmental Geology, China University of Geosciences, Wuhan 430074, China
[c] International Center for Sedimentary Geochemistry and Biogeochemistry Research, Chengdu University of Technology, Chengdu 610059, China
[d] Department of Earth and Environmental Sciences, Michigan State University, East Lansing, MI 48824, USA
[e] Department of Geological Sciences, California State University, Fullerton, CA 92831, USA
[f] School of Earth Sciences, University of Melbourne, Parkville, Vic. 3010, Australia
[g] School of Earth and Environment, University of Leeds, Leeds, LS2 9JT, UK
[h] Department of Earth and Planetary Sciences, University of California, Riverside, CA 92521, USA
*Corresponding author. Tel: +86-28-84079807; Email address: chaoli@cdut.edu.cn

Abstract

Phosphorus is a limiting nutrient that is thought to control oceanic oxygen levels to a large extent [1-3]. A possible increase in marine phosphorus concentrations during the Ediacaran Period (~635-539 Myr) has been proposed as a driver for increasing oxygen levels [4-6]. Little is known, however, about the nature and evolution of phosphorus cycling during this time [4]. Here we use carbonate-associated phosphate (CAP) from six globally-distributed sections to reconstruct oceanic phosphorous concentrations during a large negative carbon isotope excursion – the Shuram Excursion (SE), which co-occurred with global oceanic oxygenation [7-9]. Our data suggest pulsed increases in oceanic phosphorus concentrations during the falling and rising limbs of the SE. Using a quantitative biogeochemical model, we propose that this observation could be explained by carbon dioxide and phosphorus release from marine organic matter oxidation primarily by sulphate, with additional phosphorus release from carbon dioxide-driven weathering on land. Collectively, this may have resulted in elevated organic-pyrite burial and ocean oxygenation. Our CAP data also seem to suggest equivalent ocean phosphorus concentrations under maximum and minimum extents of ocean anoxia across the SE. This observation may reflect decoupled phosphorus and ocean anoxia cycles, as opposed to their coupled nature in the modern ocean. Our findings point to external stimuli such as sulphate weathering rather than internal oceanic phosphorus-oxygen cycling alone as a possible control on oceanic oxygenation in the Ediacaran, and in turn this may help explain the prolonged rise of atmospheric oxygen levels.

Phosphorus (P) is considered the primary limiting nutrient for marine productivity on geological timescales [1]. Consequently, it has been proposed that the coupled cycling of P and oxygen (O_2) maintains oxygen availability over million-year timescales, preventing runaway ocean anoxia in the Phanerozoic (<539 Myr ago) [1-3] and, whereby sustaining oxygen-demanding eukaryotic life. This relationship exists because dissolved P and O_2 follow negative feedback cycles, where higher oceanic P concentrations under ocean anoxia enhance photosynthetic production of oxygen, which oxygenates previously anoxic water masses [1,2]. This feedback arises due to release of P from both the decomposition of organic matter and iron (Fe) (oxyhydr)oxides in anoxic sediments [10]. Under oxygenated bottom waters, this released P generally becomes trapped in the sediment via a variety of pathways, including uptake by Fe (oxyhydr)oxides, biological sequestration of polyphosphates [2,10], or formation of authigenic phosphate minerals, all of which prevent the return of P to the oceans [10]. Under anoxic bottom waters, a proportion of the mobilised P can diffuse out of the sediment [11], however, enhanced organic matter preservation [11] and iron mineral formation under ferruginous (anoxic and Fe^{2+}-containing) conditions [12] can aid P retention in the sediments. Consequently, euxinic conditions (anoxic and sulphidic) are particularly conducive to sedimentary P release because of uptake of dissolved iron as sulphide minerals, thereby limiting P sequestration by iron minerals [12].

The coupled cycling of P and O_2 may have supported high levels of ocean P in the largely anoxic Precambrian oceans (>539 Myr ago) [13], as interpreted from P/Fe ratios in iron-formations [14]. Conversely, alternative interpretations of this P/Fe record suggest low oceanic P [15,16], due to effective drawdown of P by iron minerals and sequestration under ferruginous conditions [15,17]. Alternatively, low P Precambrian oceans may have arisen due to a lack of oxidants, such as oxygen

and sulphate, which suppressed P release from organic matter [4,5]. Some researchers have speculated that these low marine P levels substantially increased during the Ediacaran in conjunction with extensive deep ocean oxygenation, giving rise to modern-like oceanic P levels [4-6]. The Ediacaran P cycle is thus key to any understanding of how the interaction of P and O_2 cycles evolved from the Precambrian to the modern world and its potential role in the co-evolution of atmospheric O_2 and complex life. However, little is known about the nature and evolution of the Ediacaran P cycle. To shed light on the Ediacaran P cycle, we use the newly developed Carbonate Associated Phosphate (CAP) proxy to directly document variability in oceanic phosphate concentrations during a major Ediacaran ocean oxygenation event [7-9,18]. This episode witnessed major diversification of multicellular eukaryotic and metazoan life [18,19] and the largest known negative carbonate-carbon isotope ($\delta^{13}C_{carb}$) excursion in Earth's history, referred to here as the Shuram Excursion (SE).

We analysed six globally distributed and well-preserved carbonate sections (Fig. 1a; see Methods) to capture oceanic phosphate variability during the SE: the Jiulongwan and Sishang sections of the Doushantuo and Dengying formations from South China, the Mochia-Khutuk section of the Shuiquan formation in North-western China, the Cerro Rajón section of the Clemente, Pitiquito and Gamuza formations of northern Mexico, the Death Valley section of the Johnnie Formation of South-western USA, and the Parachilna Gorge section of the Wonoka Formation of South Australia. All sections preserve >10‰ shifts in $\delta^{13}C_{carb}$ values characteristic of the SE (Fig. 1b-g) [20-27]. The six sections reported here are taken to represent global expressions of the SE and are temporally correlated via a combination of chemostratigraphy, fossil assemblages, lithological correlation and palaeomagnetism (see Supplementary Information 2).

Among all the measured sections, CAP shows a similar “M-shape” pattern, which is broadly coincident with four stages in the temporal evolution of the $\delta^{13}C_{carb}$ trend at each section (Stage I-IV; Fig. 1b-g). Note, that the Death Valley and Parachilna Gorge sections do not preserve the final recovery and initial drop in $\delta^{13}C_{carb}$ of the SE, respectively, and the Sishang section is faulted in the middle (Fig. 1d-e, g); however, the sections capture three out of the four CAP shifts identified in other global sections. In Stage I (falling limb of the SE), there is a large increase in CAP (“P-1st” in Fig. 1) at the onset of declining $\delta^{13}C_{carb}$ values, with CAP values reaching between 0.39 and 1.33 mmol/mol [CAP/(Ca+Mg)]. This increase is followed by an equally large decrease in CAP to a minimum during the mid-SE (Stage II; the plateau in SE $\delta^{13}C_{carb}$ values), with CAP values ranging between 0.03 and 0.24 mmol/mol. A rebound in CAP begins in the mid-SE (Stage II) and continues to increase as $\delta^{13}C_{carb}$ values increase toward the termination of the SE, reaching values of 0.32 to 2.18 mmol/mol (Stage III; rising limb of the SE; “P-2nd” in Fig. 1)), which is then followed by a gradual decline in CAP values to between 0.07 and 0.20 mmol/mol following the termination of the SE (Stage IV; a return to pre-SE $\delta^{13}C_{carb}$ values). Given that the CAP trends in all sections are connected to the $\delta^{13}C_{carb}$ excursion, and since the SE is approximately synchronous [28], a broadly contemporaneous shift in global oceanic P levels is implied.

CAP can be used to produce direct estimates of relative changes in palaeoceanic phosphate levels at the time of carbonate precipitation, if contamination, diagenetic alteration and other potential changes in oceanic chemistry can be evaluated [29]. Our CAP extractions show no signs of contamination by other sources of sedimentary P, as there is little to no correlation between CAP and bulk rock P, total organic carbon (TOC) or La (an element used for tracking phosphate mineral dissolution [29,30]) (Extended Data Table 1; see Supplementary Information 3). Encouragingly, an

independent methodology using in-situ analysis of CAP in carbonate preserving primary textures gives trends consistent with our bulk CAP data from the Dengying Fm. in the Jiulongwan section of South China (Fig. 1b) [30].

While the global occurrence of our CAP trends is difficult to reconcile with diagenetic alteration, globally synched diagenetic alteration of carbonate has been purported to result after marine regression exposes platforms to meteoric waters [31]. The SE, however, is recognised as a marine transgression event, which is unlikely to expose carbonate sediments to meteoric alteration [32]. Nevertheless, in order to assess the potential effects of diagenetic alteration on CAP we utilise an open-system diagenetic model to evaluate chemical signals of alteration (Extended Data Fig. 1). Our diagenetic model shows that CAP is altered at similar or greater fluid-to-rock ratios than a number of carbonate proxies, such as $\delta^{13}C_{carb}$, $\delta^{18}O$, $\delta^{44/40}Ca$ or Mn/Sr. Therefore, CAP could correlate with these proxies across the SE if altered, but this is not observed in our samples (Extended Data Table 1; Fig. 1) [29,30]. Furthermore, coexisting $\delta^{34}S$ values in Carbonate-Associated Sulphate ($\delta^{34}S_{CAS}$) decline throughout the SE [20-22,24] (Fig. 1b-d), which is inconsistent with known diagenetic pore water chemistry and the increasingly elevated $\delta^{34}S_{CAS}$ values that commonly occur in diagenetic carbonates due to microbial sulphate reduction [33]. In addition, local redox proxies (e.g., I/(Ca+Mg), Ce/Ce*, Fe-speciation) measured among globally distributed SE sections record differing local redox conditions [34-36], which is also inconsistent with a global diagenetic pathway (see Supplementary Information 3). Finally, $^{87}Sr/^{86}Sr$ values and trends in the Cerro Rajón and Death Valley sections reflect local diagenetic alteration (see Supplementary Information 2) yet preserve similar CAP trends to other SE sections (Fig. 1).

Importantly, calcite and dolomite minerals in the study sections have undergone different

diagenetic pathways and may have differences in distribution coefficients for CAP [28]. Despite this, CAP trends remain consistent among sections regardless of whether they are hosted in calcite or dolomite minerals (Fig. 1b-g). This strongly argues against a dominant diagenetic and mineralogical control on the CAP trends, and therefore we conclude that the CAP trends observed in this study most likely represent primary changes in seawater chemistry although diagenetic alteration of local CAP values may have exerted a minor influence. However, we note that in addition to diagenetic processes, changes in ocean pH, alkalinity, temperature and carbonate precipitation can all impact CAP values without concomitant changes in oceanic phosphate concentrations. We consider all of these potentially impacting factors on our CAP data in Supplementary Information 3, 4 and 9, and find that changes in oceanic phosphate concentration is the most plausible overarching control on the global CAP trends that we observed, albeit with possible minor overprints from changes in seawater chemistry.

Given the lower-than-mantle $\delta^{13}C_{carb}$ values of the SE, some models which report the SE as a primary-seawater-signal have centred on oxidation of an organic matter reservoir, such as dissolved organic matter (DOM) [37,38], fossil kerogen [23], or methane [39], all of which contain ^{13}C-depleted carbon, and with the exception of methane, also contain P. Assuming oxidant supply exceeds demand, these models are supported by many redox studies which suggest a transient global oceanic oxidation event during the SE, as supported by potential global-scale redox proxies such as $\delta^{238}U_{carb}$ (Fig. 1b-d). Other models have invoked a diagenetic origin or air-sea exchange of CO_2 [32] for the low $\delta^{13}C_{carb}$ values of the SE [31,40], but it is difficult to envisage how these models could reconcile the co-evolving trends of our new CAP data with the $\delta^{13}C_{carb}$ and redox proxy trends of the SE (see Supplementary Information 3 and 7).

Here we entertain a number of primary seawater signal hypotheses for the SE (see Supplementary Information 7 and Extended Data Fig. 2 for details). As discussed below, we find that a best-fit solution is achieved when rising oceanic sulphate levels (driven by enhanced weathering) stimulates sulphate-limited microbial sulphate reduction and oxidation of a DOM reservoir [37] (Fig. 2). This mechanism is supported by higher values of Carbonate-Associated Sulphate (CAS) concentration and lower values of $\delta^{34}S_{CAS}$ during the SE (Fig. 1b-d) [20-24], which are indicative of a growing oceanic sulphate reservoir [37]. Enhanced weathering (and accordingly sulphate supply) during the SE is supported by elevated $^{87}Sr/^{86}Sr$ [41] (Fig. 1b-e) and εNd(t) records [42]. We quantitatively explore this scenario and its impact on ocean P using the COPSE biogeochemical model (Fig. 3; Extended Data Figs. 2-7).

It is well documented that the Ediacaran oceans were dominated by deeper anoxic waters [43,44], and therefore free oxygen would have been in contact with a small fraction of the deep-ocean DOM pool. Consequently, sulphate is the primary oxidant in our model. Indeed, if a DOM reservoir was oxidised by free oxygen, our modeling indicates that ocean anoxia would not significantly decrease during the SE, which would allow for sustained high ocean P levels resulting from elevated weathering and DOM oxidation (Extended Data Fig. 3). However, this contrasts with coexisting $\delta^{238}U_{carb}$ data showing a substantial decrease in ocean anoxia, as well as the CAP records showing a drop in oceanic P levels during the SE [8,35] (Fig. 1b-g). Similarly, models for DOM oxidation by a combination of sulphate and free oxygen are also inconsistent with the observed $\delta^{238}U_{carb}$-CAP records (Extended Data Fig. 3).

The sizes of the modelled DOM reservoir and sulphate pulse to the oceans were adjusted to produce a SE with a duration of 15 Myr (see Supplementary Information 5), while also reproducing

the two observed CAP peaks (Extended Data Figs. 4-6; P-1st and P-2nd in Fig. 1). Varying the magnitude of the additional sulphate pulse to the oceans has little effect on modelled CAP trends, while burying all additional sulphate as pyrite creates a pO_2 trend inconsistent with redox proxies from the SE (Extended Data Fig. 5). Similarly, if gypsum is assumed not to covary with seawater sulphate levels, increasing sulphate levels prevent a return to anoxia after the SE, which is inconsistent with coexisting $\delta^{238}U_{carb}$ and $\delta^{34}S_{CAS}$ records (Extended Data Fig. 5) . Finally, to best fit our CAP data, we suppressed oceanic P levels in COSPE under anoxia by assuming that P is also buried in association with Fe^{2+}, rather than only with Fe^{3+} (Fig. 3; also see Extended Data Fig. 7 for model results with no Fe^{2+}-associated P burial). This choice is based on the predominantly ferruginous ocean conditions in the late Neoproterozoic and previous suggestions that ferruginous oceans may have drawn down ocean P through uptake via a variety of Fe mineral precipitates [6,15,17]. The relative magnitudes of the modelled ocean P peaks were varied by changing the onset and waning of Fe^{2+}-P burial and whether HCO_3^- is released alongside CO_2 during sulphate reduction of DOM (Fig. 3). Details and rationale for the model choices are provided in the Methods section and Supplementary Information 6-8.

Our quantitative modelling indicates that the SE CAP profiles may have recorded feedbacks in weathering, organic matter burial/oxidation, and the extent of marine anoxia that bridges previously elusive $\delta^{13}C$ and palaeoredox proxy relationships. We detail the scenario below: (1) Additional sulphate input to the oceans from weathering triggers the oxidation of a DOM reservoir by sulphate at the beginning of the SE (Fig. 2a). This released organic-bound C and P, which led to declining oceanic $\delta^{13}C$ and increased oceanic P as well as atmospheric pCO_2, thereby elevating P input to the oceans via silicate weathering (Stage I and P-1st in Figs. 1b-g, 3b). CO_2-driven weathering also

196 resulted in an elevated $^{87}Sr/^{86}Sr$ curve across the SE (Figs. 1b-e, 3d) [41]. (2) Greater P availability
197 would then elevate primary productivity and concomitant organic matter and pyrite burial, which
198 increased pO_2 (Fig. 2a) and decreased the extent of ocean anoxia (Fig. 2b), as suggested by the
199 observed global shift to more positive $\delta^{238}U$ values (Figs. 1b-d; 3c). (3) A decrease in ocean anoxia
200 would increase P burial and lead to a decrease in the oceanic P reservoir (Fig. 2b), consistent with
201 declining CAP values, and coincident maximum $\delta^{238}U$ values (Stage II in Figs. 1b-g, 3b-c). (4) As
202 the size of the DOM reservoir dwindled, oceanic $\delta^{13}C$ would start to return to pre-SE values (Stage
203 III in Figs. 1b-g, 3a). Simultaneously, decreasing organic and pyrite burial drove atmospheric oxygen
204 lower, which supported by a reduced P reservoir and consequently lower rates of oxygenic
205 photosynthesis, resulted in lower pO_2 levels and increasing marine anoxia (Fig. 2c), which may be
206 recorded by a transition to increasingly negative $\delta^{238}U$ values (Stage III in Figs. 1b-d and 3c) [8,45].
207 Other independent carbonate- and siliclastic-hosted redox proxies (e.g., Tl and Mo isotopes [46,47],
208 carbonate-bound iodate [35] and Fe-speciation [36]), corroborate the increase after a prior decrease in
209 ocean anoxia across the SE. Increasing ocean anoxia would decrease P burial, which, when
210 coupled to continued P release from DOM and weathering, would lead to another increase in the P
211 reservoir (Fig. 2c), as observed in the CAP data (P-2nd in Figs. 1b-g, 3b). (5) Finally, cessation of
212 massive DOM oxidation and reduced continental weathering led to a waning P input from DOM and
213 continental weathering, which in turn decreased organic and pyrite burial supporting a return of
214 elevated anoxia, as evidenced by negative $\delta^{238}U$ values during the terminal SE in multiple global
215 carbonate sections[7,9] and a return to pre-SE $\delta^{13}C_{carb}$ values and coexisting low CAP values (Stage
216 IV in Figs. 1b-g and 3a-c).

217 An alternative to DOM oxidation could be methane oxidation [23] by sulphate. However, anaerobic

218 oxidation of methane is less likely because methane oxidation will not release P directly and is
219 unlikely to lead to pCO_2 increases (and thus elevated P weathering) —favouring alkalinity increases
220 instead. The possibility of small temporal differences in our $\delta^{13}C_{carb}$ and CAP trends among globally
221 distributed sections (Fig. 1) may have resulted from heterogeneous redox conditions in the
222 Ediacaran which led to variable spatiotemporal rates of DOM oxidation, continental weathering and
223 element cycling [22]. Consequently, we conclude that our CAP data in cohort with coexisting C, S, and
224 U isotopic data, as well as other redox proxies, are best explained by the oxidation of an organic
225 matter reservoir (DOM or fossil organic matter) by sulphate and resulting organic and pyrite burial,
226 which facilitated ocean oxygenation and perhaps the coeval diversification of complex life in the
227 Ediacaran (Fig. 3e) [18,19].

228 The CAP proxy predominantly records local seawater P levels, reflecting P fluxes from
229 surrounding sediments, riverine input, ocean upwelling etc. Whether local seawater P levels are
230 controlled by local or global processes will depend on the magnitude of fluxes involved at different
231 timescales. Observations of long-term oceanic P cycling suggest that upwelling of deep ocean P
232 onto continental shelves is quantitatively larger than local continental shelf P fluxes [10]. This can be
233 demonstrated using a quantitative four-box ocean P cycle model which predicts that continental
234 shelf P concentrations, aside from the most proximal areas and mixed layer, track deep ocean P
235 levels over geological timescales, due to the supply from upwelling [3,13] (Extended Data Fig. 8). Given
236 the relatively homogenous concentration of deep ocean P, and a residence time greater than the
237 oceanic mixing time [10], upwelling of deep ocean P is expected to result in continental shelf P
238 concentrations that capture overall P levels in the global ocean when viewed over geological
239 timescales. Consequently, our CAP trends from continental shelves are expected to represent global

changes in the average ocean P concentration over geological timescales, and their global relationships are thus preserved despite the potential for local overprints that include redox controls on continental shelf P concentrations (see Supplementary Information 8). This view is supported by similar CAP trends among our global sections, despite having been deposited under differing local redox conditions [34,35].

Given that CAP and $\delta^{238}U_{carb}$ trends may reflect relative changes in the average global ocean P concentration and extent of ocean floor anoxia respectively, our study provides a unique opportunity to explore dynamics in the Ediacaran P and O_2 cycles. As predicted by observations of modern aquatic environments, expansion of oxygenated bottom waters during the SE (evidenced by $\delta^{238}U_{carb}$) should be accompanied by declines in marine P concentration (as seen in CAP). Surprisingly, however, minimal extents of ocean floor anoxia (i.e., the most positive $\delta^{238}U_{carb}$ values in Stage II of the SE) are associated with CAP values of equal magnitude to those CAP values during periods of maximum ocean floor anoxia before/ after the SE (i.e., the most negative $\delta^{238}U_{carb}$ values in the early Stage I and Stage IV) at all studied sections (Fig. 1b-d). This observation is in stark contrast to modern P and O_2 cycling where widespread ocean floor anoxia supports higher ocean P levels relative to periods with limited ocean floor anoxia. Similarly, $\delta^{238}U_{carb}$ and CAP co-vary, increasing and decreasing at the start and end of the SE, respectively (Fig. 1b-e), which also contrasts with canonical models of modern P and O_2 cycles. This difference indicates that the Ediacaran P and O_2 cycles may have been fundamentally differed to the modern (Fig. 3b-c; Extended Data Fig. 7) [1-3,11]. Note that, this conclusion is based on the comparison of CAP values from discrete intervals when $\delta^{238}U_{carb}$ data are at their maximum and minimum, and therefore a precise temporal correlation of CAP trends among the studied sections does not affect the

conclusions. Moreover, CAP and $\delta^{238}U_{carb}$ were measured in identical sample powders and minerals, ruling out effects of temporal or mineralogical differences.

One may argue that P fluxes from continental weathering and organic matter oxidation could have maintained high ocean P levels during the SE, effectively balancing the increased P sinks under oxygenated bottom waters. However, current quantitative models of P and O_2 cycling, indicate that even under the most extreme P input fluxes, oceanic P levels are still expected to be lower during minimal oceanic anoxia during the SE, relative to before or after the SE when the extent of seafloor anoxia was greater (see Extended Data Fig. 4 and Supplementary Information 9). Additionally, modeling and experimental results suggest that changes in pH, alkalinity or carbonate precipitation rate resulting from shifts in surface weathering, pCO_2 and organic remineralisation are unlikely to have decoupled the CAP and $\delta^{238}U_{carb}$ values (see Extended Data Fig. 9 and Supplementary Information 4 and 9).

The roughly equivalent oceanic P levels under maximum and minimum extents of ocean floor anoxia across the SE provides the first direct observation for a decoupling of the modern-style negative feedback cycles between oceanic P and O_2. Currently there are no other coupled datasets of CAP and $\delta^{238}U_{carb}$ which capture a modern-style P and O_2 cycle that we can compare our dataset to. However, chemical traits of redox-dependant phosphorus burial are frequently observed in Phanerozoic sediments [2,11,12], but largely absent in Ediacaran sediments deposited under ferruginous conditions [48], which may support our conclusion of decoupled P and O_2 cycles in Ediacaran oceans. For example, C_{org}/ P_{Tot} (total sediment organic carbon/ total sediment P) values are roughly invariant among siliciclastic sediments deposited under variable redox conditions in the

283 Ediacaran Doushantuo Formation [48], whereas C_{org}/ P_{Tot} commonly covaries with local redox
284 conditions in Phanerozoic sediments [2,11,12].

285 While we favour a primary seawater signal as described above, and cannot entirely rule out an
286 early diagenetic interpretation of the CAP trends, such a scenario is unlikely to change our
287 conclusion of decoupled P and O_2 cycling in the Ediacaran Ocean. This is because in modern marine
288 sediments, increasingly ^{13}C-depleted pore waters carry increasingly higher P concentrations
289 following the remineralisation of organic matter. Therefore, if carbonate deposited during the SE
290 indeed captured diagenetic porewater chemistry, the more ^{13}C-depleted fluids (down to −12‰)
291 should have carried higher solution P concentrations relative to fluids surrounding carbonate
292 deposited before or after the SE with high $\delta^{13}C_{carb}$ values (up to +5‰). However, carbonates with
293 these endmember $\delta^{13}C_{carb}$ values across the SE carry equable CAP values (Fig. 1b-g). According
294 to our early diagenetic model (Supplementary Information 3), in order to achieve a $\delta^{13}C_{carb}$ shift from
295 +5 to −12‰ in diagenetic carbonates, CAP is expected to increase by at least a factor of four yet
296 plots of our $\delta^{13}C_{carb}$ and CAP data show no such trend (Extended Data Fig. 1d). This decoupling
297 between $\delta^{13}C_{carb}$ and CAP required substantial sequestration of P released from diagenetic organic
298 remineralisation in reducing Ediacaran pore waters (directly evidenced by bottom-water redox
299 proxies, e.g., Fe speciation data across the interval of highly depleted $\delta^{13}C$ values in the Jiulongwan
300 section [43]). This P sequestration in anoxic porewaters (and Ediacaran water columns) [43,44] is also in
301 stark contrast to modern P and O_2 cycling, thus supporting a decoupled P and O_2 cycle in the
302 Ediacaran (see more detailed discussion in Supplementary Information 3). Moreover, purported
303 models for the SE which achieve low $\delta^{13}C$ in seawater via non-DOM-oxidation mechanisms [32] still
304 advocate for carbonate deposited during the SE to have captured seawater chemistry. Consequently,

the observed CAP and $\delta^{238}U_{carb}$ trends would be faithful recorders of seawater chemistry and therefore support the conclusion of decoupled P and O_2 cycles in the Ediacaran.

The decoupling of ocean P recycling and anoxia observed here likely results from persistent P removal by organic or iron mineral phases under widespread oxidant-depleted, ferruginous conditions in Ediacaran Oceans [16]. Given similar redox conditions and potentially a small P reservoir in Precambrian oceans preceding the Ediacaran [49], it is reasonable to infer that such a decoupling of the P and O_2 cycles may have existed throughout most of the Precambrian [50]. Importantly, a weakening of the oceanic P and O_2 feedbacks as suggested here would have locked the Precambrian oceans and atmosphere into a largely anoxic state, because ocean anoxia would not have resulted in elevated marine P availability, oxygenic photosynthesis and organic matter burial relative to periods of lower marine anoxia. Consequently, Precambrian oceanic oxygenation events, such as the SE and maybe others (e.g., the Great Oxygenation Event [50]), may have relied on external stimuli such as sulphate weathering inputs rather than internal oceanic P-O_2 cycling alone [4,5]. This may explain the prolonged rise of oxygen and complex life over Earth history until the removal of widespread ferruginous conditions or increases in sulphate/oxidant availability in the Phanerozoic which shifted the Ediacaran P and O_2 cycles into a modern-style, negative feedback cycle [1]. In turn this transition may explain the prolonged oxygenation and metazoan habitation of the Phanerozoic oceans [1].

Acknowledgements

We thank Bing Shen and Ruimin Wang for generously providing samples from the Mochia-Khutuk section and Lei Zheng for assistance in obtaining the Sishang section samples. This study was supported by the NSFC (grants # 41825019, 42130208, 41821001), and the National Key Research and Development Program of China (2022YFF0800102) for funding. M.S.D. acknowledges support from the International Exchange Program for Postdoctors of China and

funding from the China Postdoctoral Science Foundation. Additional funding through the NASA Astrobiology Institute under Cooperative Agreement No. NNA15BB03A issued through the Science Mission Directorate and the Interdisciplinary Consortia for Astrobiology Research (T.W.L.).

Author Contributions

C.L led the research. C.L and M.S.D designed the research. M.S.D, Z.Z, M.C and H.G performed analyses. W.S and B.J.W.M conducted modelling work. C.L, T.W.L, D.S.H, S.J.L, M.W.W, A.vS.H, K.L, M.C, H.G provided samples and assistance in the field. S.W.P provided analytical assistance. M.S.D, C.L, and W.S wrote the manuscript with important discussion and contributions from all authors.

Data Availability Statement

All data generated or analysed during this study are available at https://figshare.com/articles/dataset/Dodd_et_al_2023_xlsx/22274293 and included with the published article (and its supplementary information files).

Materials Availability

All samples were collected and exported in a responsible manner and in accordance with relevant permits and local laws. Global coordinates and/ or location information and drill core names are given for all samples collected in the supplementary information files. Requests for materials should be addressed to C.L.

References

1 Van Cappellen, P. & Ingall, E. D. Redox Stabilization of the Atmosphere and Oceans by Phosphorus-Limited Marine Productivity. *Science* **271**, 493-496, doi:10.1126/science.271.5248.493 (1996).

2 Algeo, T. J. & Ingall, E. Sedimentary Corg:P ratios, paleocean ventilation, and Phanerozoic atmospheric pO2. *Palaeogeography, Palaeoclimatology, Palaeoecology* **256**, 130-155, doi:10.1016/j.palaeo.2007.02.029 (2007).

3 Slomp, C. P. & Van Cappellen, P. The global marine phosphorus cycle: sensitivity to oceanic circulation. *Biogeosciences* **4**, 155-171, doi:10.5194/bg-4-155-2007 (2007).

4 Laakso, T. A., Sperling, E. A., Johnston, D. T. & Knoll, A. H. Ediacaran reorganization of the marine phosphorus cycle. *Proceedings of the National Academy of Sciences* **117**, 11961, doi:10.1073/pnas.1916738117 (2020).

5 Kipp, M. A. & Stüeken, E. E. Biomass recycling and Earth's early phosphorus cycle. *Science Advances* **3**, doi:10.1126/sciadv.aao4795 (2017).

6 Reinhard, C. T. *et al.* Evolution of the global phosphorus cycle. *Nature* **541**, 386-389, doi:10.1038/nature20772 (2017).

7 Zhang, F. *et al.* Extensive marine anoxia during the terminal Ediacaran Period. *Science*

Advances **4**, eaan8983, doi:10.1126/sciadv.aan8983 (2018).

8 Zhang, F. *et al.* Global marine redox changes drove the rise and fall of the Ediacara biota. *Geobiology* **17**, 594-610, doi:10.1111/gbi.12359 (2019).

9 Tostevin, R. *et al.* Uranium isotope evidence for an expansion of anoxia in terminal Ediacaran oceans. *Earth and Planetary Science Letters* **506**, 104-112, doi:https://doi.org/10.1016/j.epsl.2018.10.045 (2019).

10 Ruttenberg, K. C. in *Treatise on Geochemistry* (eds Heinrich D. Holland & Karl K. Turekian) 585-643 (Pergamon, 2003).

11 Ingall, E. D., Bustin, R. M. & Van Cappellen, P. Influence of water column anoxia on the burial and preservation of carbon and phosphorus in marine shales. *Geochimica et Cosmochimica Acta* **57**, 303-316, doi:https://doi.org/10.1016/0016-7037(93)90433-W (1993).

12 Xiong, Y. *et al.* Phosphorus cycling in Lake Cadagno, Switzerland: A low sulfate euxinic ocean analogue. *Geochimica et Cosmochimica Acta* **251**, 116-135, doi:https://doi.org/10.1016/j.gca.2019.02.011 (2019).

13 Alcott, L. J., Mills, B. J. W. & Poulton, S. W. Stepwise Earth oxygenation is an inherent property of global biogeochemical cycling. *Science* **366**, 1333-1337 (2019).

14 Planavsky, N. J. *et al.* The evolution of the marine phosphate reservoir. *Nature* **467**, 1088-1090, doi:10.1038/nature09485 (2010).

15 Bjerrum, C. J. & Canfield, D. E. Ocean productivity before about 1.9Gyr ago limited by phosphorus adsorption onto iron oxides. *Nature* **417**, 159-162, doi:http://www.nature.com/nature/journal/v417/n6885/suppinfo/417159a_S1.html (2002).

16 Jones, C., Nomosatryo, S., Crowe, S., Bjerrum, C. J. & Canefield, D. E. Iron oxides, divalent cations, silica, and the early earth phosphorus crisis. *Geology* **43**, 135-138, doi:10.1130/G36044.1 (2015).

17 Derry, L. A. Causes and consequences of mid-Proterozoic anoxia. *Geophysical Research Letters* **42**, 8538-8546, doi:10.1002/2015gl065333 (2015).

18 Evans, S. D., Diamond, C. W., Droser, M. L. & Lyons, T. W. Dynamic oxygen and coupled biological and ecological innovation during the second wave of the Ediacara Biota. *Emerging Topics in Life Sciences* **2**, 223-233, doi:10.1042/ETLS20170148 (2018).

19 Darroch, S. A. F., Smith, E. F., Laflamme, M. & Erwin, D. H. Ediacaran Extinction and Cambrian Explosion. *Trends in Ecology & Evolution* **33**, 653-663, doi:https://doi.org/10.1016/j.tree.2018.06.003 (2018).

20 Fike, D. A., Grotzinger, J. P., Pratt, L. M. & Summons, R. E. Oxidation of the Ediacaran ocean. *Nature* **444**, 744-747, doi:10.1038/nature05345 (2006).

21 Shi, W. *et al.* Sulfur isotope evidence for transient marine-shelf oxidation during the Ediacaran Shuram Excursion. *Geology* **46**, 267-270, doi:10.1130/g39663.1 (2018).

22 Li, C. *et al.* Uncovering the spatial heterogeneity of Ediacaran carbon cycling. *Geobiology* **15**, 211-224, doi:10.1111/gbi.12222 (2017).

23 Kaufman, A. J., Corsetti, F. A. & Varni, M. A. The effect of rising atmospheric oxygen on carbon and sulfur isotope anomalies in the Neoproterozoic Johnnie Formation, Death Valley, USA. *Chemical Geology* **237**, 47-63, doi:https://doi.org/10.1016/j.chemgeo.2006.06.023 (2007).

24 Loyd, S. J. *et al.* Sustained low marine sulfate concentrations from the Neoproterozoic to the Cambrian: Insights from carbonates of northwestern Mexico and eastern California. *Earth and Planetary Science Letters* **339-340**, 79-94, doi:https://doi.org/10.1016/j.epsl.2012.05.032 (2012).

413 25 Merdith, A. S. *et al.* A full-plate global reconstruction of the Neoproterozoic. *Gondwana Research* **50**, 84-134, doi:https://doi.org/10.1016/j.gr.2017.04.001 (2017).
415 26 Huang, K. *et al.* Interaction of Shibantan Biota and environment in the terminal Ediacaran ocean: Evidence from I/(Ca+Mg) and sulfur isotopes. *Precambrian Research* **379**, 106814, doi:https://doi.org/10.1016/j.precamres.2022.106814 (2022).
418 27 Wang, R. *et al.* A 20 million-year Great Ediacaran Glaciation witnessed the rise of the earliest animals. *Preprint (Version 1) available at Research Square* doi:[https://doi.org/10.21203/rs.3.rs-793746/v1] (2021).
421 28 Rooney, A. D. *et al.* Calibrating the coevolution of Ediacaran life and environment. *Proceedings of the National Academy of Sciences*, 202002918, doi:10.1073/pnas.2002918117 (2020).
424 29 Dodd, M. S. *et al.* Development of carbonate-associated phosphate (CAP) as a proxy for reconstructing ancient ocean phosphate levels. *Geochimica et Cosmochimica Acta* **301**, 48-69, doi:10.1016/j.gca.2021.02.038 (2021).
427 30 Shimura, T. *et al.* In-situ analyses of phosphorus contents of carbonate minerals: Reconstruction of phosphorus contents of seawater from the Ediacaran to early Cambrian. *Gondwana Research* **25**, 1090-1107, doi:10.1016/j.gr.2013.08.001 (2014).
430 31 Swart, P. K. & Kennedy, M. J. Does the global stratigraphic reproducibility of δ 13 C in Neoproterozoic carbonates require a marine origin? A Pliocene–Pleistocene comparison. *Geology* **40**, 87-90 (2012).
433 32 Busch, J. F. *et al.* Global and local drivers of the Ediacaran Shuram carbon isotope excursion. *Earth and Planetary Science Letters* **579**, 117368, doi:https://doi.org/10.1016/j.epsl.2022.117368 (2022).
436 33 Loyd, S. J., Berelson, W. M., Lyons, T. W., Hammond, D. E. & Corsetti, F. A. Constraining pathways of microbial mediation for carbonate concretions of the Miocene Monterey Formation using carbonate-associated sulfate. *Geochimica et Cosmochimica Acta* **78**, 77-98, doi:https://doi.org/10.1016/j.gca.2011.11.028 (2012).
440 34 Cheng, M. *et al.* Barite in the Ediacaran Doushantuo Formation and its implications for marine carbon cycling during the largest negative carbon isotope excursion in Earth's history. *Precambrian Research* **368**, 106485, doi:https://doi.org/10.1016/j.precamres.2021.106485 (2022).
444 35 Hardisty, D. S. *et al.* Perspectives on Proterozoic surface ocean redox from iodine contents in ancient and recent carbonate. *Earth and Planetary Science Letters* **463**, 159-170, doi:https://doi.org/10.1016/j.epsl.2017.01.032 (2017).
447 36 Wood, R., Bowyer, F., Penny, A. & Poulton, S. W. Did anoxia terminate Ediacaran benthic communities? Evidence from early diagenesis. *Precambrian Research* **313**, 134-147, doi:https://doi.org/10.1016/j.precamres.2018.05.011 (2018).
450 37 Shields, G. A. *et al.* Unique Neoproterozoic carbon isotope excursions sustained by coupled evaporite dissolution and pyrite burial. *Nature Geoscience* **12**, 823-827, doi:10.1038/s41561-019-0434-3 (2019).
453 38 Rothman, D. H., Hayes, J. M. & Summons, R. E. Dynamics of the Neoproterozoic carbon cycle. *Proceedings of the National Academy of Sciences* **100**, 8124, doi:10.1073/pnas.0832439100 (2003).
456 39 Bjerrum, C. J. & Canfield, D. E. Towards a quantitative understanding of the late Neoproterozoic carbon cycle. *Proceedings of the National Academy of Sciences* **108**, 5542,

doi:10.1073/pnas.1101755108 (2011).
40 Derry, L. A. A burial diagenesis origin for the Ediacaran Shuram–Wonoka carbon isotope anomaly. *Earth and Planetary Science Letters* **294**, 152-162, doi:https://doi.org/10.1016/j.epsl.2010.03.022 (2010).
41 Sawaki, Y. *et al.* The Ediacaran radiogenic Sr isotope excursion in the Doushantuo Formation in the Three Gorges area, South China. *Precambrian Research* **176**, 46-64, doi:https://doi.org/10.1016/j.precamres.2009.10.006 (2010).
42 Wei, G.-Y. *et al.* Long-term evolution of terrestrial inputs from the Ediacaran to early Cambrian: Clues from Nd isotopes in shallow-marine carbonates, South China. *Palaeogeography, Palaeoclimatology, Palaeoecology* **535**, 109367, doi:https://doi.org/10.1016/j.palaeo.2019.109367 (2019).
43 Li, C. *et al.* A Stratified Redox Model for the Ediacaran Ocean. *Science* **328**, 80, doi:10.1126/science.1182369 (2010).
44 Canfield, D. E. *et al.* Ferruginous Conditions Dominated Later Neoproterozoic Deep-Water Chemistry. *Science* **321**, 949, doi:10.1126/science.1154499 (2008).
45 Li, Z. *et al.* Transient and stepwise ocean oxygenation during the late Ediacaran Shuram Excursion: Insights from carbonate δ238U of northwestern Mexico. *Precambrian Research* **344**, 105741, doi:https://doi.org/10.1016/j.precamres.2020.105741 (2020).
46 Fan, H. *et al.* Constraining oceanic oxygenation during the Shuram excursion in South China using thallium isotopes. *Geobiology* **n/a**, doi:10.1111/gbi.12379 (2020).
47 Kendall, B. *et al.* Uranium and molybdenum isotope evidence for an episode of widespread ocean oxygenation during the late Ediacaran Period. *Geochimica et Cosmochimica Acta* **156**, 173-193, doi:https://doi.org/10.1016/j.gca.2015.02.025 (2015).
48 Jin, C. *et al.* Highly heterogeneous “poikiloredox” conditions in the early Ediacaran Yangtze Sea. *Precambrian Research* **311**, 157-166, doi:https://doi.org/10.1016/j.precamres.2018.04.012 (2018).
49 Lyons, T. W., Reinhard, C. T. & Planavsky, N. J. The rise of oxygen in Earth/'s early ocean and atmosphere. *Nature* **506**, 307-315, doi:10.1038/nature13068 (2014).
50 Alcott, L. J., Mills, B. J. W., Bekker, A. & Poulton, S. W. Earth’s Great Oxidation Event facilitated by the rise of sedimentary phosphorus recycling. *Nature Geoscience* **15**, 210-215, doi:10.1038/s41561-022-00906-5 (2022).

Methods

Bulk-rock Phosphorus analysis

Although altered material could not be completely avoided, fresh pieces of only fine-grained carbonate rock were selected and crushed to a powder. Phosphorus measurements were conducted by dissolving ~50 mg of sample powder using a standard HNO_3–HF digestion protocol, in which HNO_3–HF (1:1) and HNO_3 were sequentially added to a 15-mL Teflon bomb at 190°C until complete

digestion was achieved. Distilled HNO_3 and trace metal-grade HF reagents were used for all samples. The leachates were then measured by ICP-MS using an Agilent 7700x inductively coupled plasma mass spectrometer (ICP-MS). Analytical errors were better than ±7% for phosphorus based on duplicate analyses of two USGS standards (BCR-2, BHVO-2) and two Chinese national standards (GSR1, GSR5).

Carbon analysis

Total carbon (TC) and total organic carbon (TOC) were measured using a CS-900 Carbon Analyser. TC was measured directly by weighing out ~0.1g of rock powder with iron shavings and tungsten pellets to aid combustion in the analyser. A calcium carbonate carbon standard (AR1034) was analysed after every 10 samples to check reproducibility (± 0.1 wt% C; n = 30). To measure TOC, an aliquot of sample powder (~1 g) was reacted with 6 M HCl to decarbonate the sample, rinsed with deionised water to neutral pH, then centrifuged and dried, and finally measured in the analyser as for TC. Total inorganic carbon (TIC) was then calculated by the difference between TC and TOC.

Carbonate carbon isotope analysis

About 60 to 300 μg of sample powder was loaded into a vial after drying at 70°C for 24 hr in an argon atmosphere. The samples were then reacted with 100% phosphoric acid under a vacuum at 70°C for 220 s using a Kiel IV device. The resulting CO_2 was subsequently introduced into a MAT 253 isotope ratio mass spectrometer (IRMS) for isotopic measurements. Delta values were calibrated relative to international reference standard NBS-19 ($\delta^{13}C$ = +1.95‰; $\delta^{18}O$ = −2.20‰)

518 and Chinese national standard GBW04416 ($\delta^{13}C$ = +1.61 ± 0.03‰; $\delta^{18}O$ = = 1.59 ± 0.11‰).
519 Carbon and oxygen isotope data for carbonates are reported relative to Vienna Pee Dee
520 Belemnite (VPDB) with a precision of better than ±0.1‰ based on duplicate analyses of
521 GBW04416 and the study samples.
522
523 **Carbonate-Associated Phosphate (CAP) analysis**
524 CAP was measured following previously established protocols [29]. Only samples
525 comprising >50% carbonate were chosen for analysis. Based on sample TIC and carbonate
526 mineralogy, sufficient sample powder was weighed out to yield ~1 mmol of carbonate. An
527 appropriate amount of 2% vol/vol acetic acid was then added to the powder to dissolve up to 70%
528 of the carbonate. After 30 minutes the sample was centrifuged, and the leachate was extracted. An
529 aliquot of leachate was taken for major and trace element analyses and measured using an Expec
530 6000 Inductively Coupled Plasma Optical Emission Spectrometer (ICP-OES) for Ca and Mg and an
531 Agilent 7700x ICP-MS for trace elements. Analytical errors were better than ±2% for all studied
532 elements based on duplicate analyses of two USGS standards (BCR-2, BHVO-2) and two Chinese
533 national standards (GSR1, GSR5). Another aliquot was taken and mixed with H_2SO_4 to achieve a 1
534 M H_2SO_4 concentration and left for 1 hour to remove Ca as $CaSO_4$. Then P was measured by
535 spectrophotometry using the molybdenum-blue method at a wavelength of 880 nm, with a relative
536 standard deviation of better than ±5%. The sample residue was then washed with 50ml of 10% NaCl
537 solution buffered to pH 8 with $NaHCO_3$ for 24 hours, and P was measured by the molybdenum-blue
538 method. This sequence was repeated until P in the wash was below detection limit (0.05 ppm). The
539 P in the leach and washes were then summed together to give CAP, which was then normalised to

the Ca and Mg concentrations in the leach. Three Ediacaran dolomite sediments of varying TIC and TOC were run alongside unknown samples to check reproducibility for quality assurance, repeat CAP measurements were within ±5%.

Strontium isotope analysis

The extraction method for strontium isotope analysis was based on previous works [51-53]. Around 0.1g of sample was weighed out and then washed for 24 hours in 10ml of 1M ammonium acetate buffered to pH 8 in order to remove exchangeable strontium. The sample was then centrifuged, and the wash discarded and the sample rinsed with Milli-Q water. Subsequently the sample was partially leached in 2% acetic acid to dissolve 30% of the sample carbonate and left to react overnight. The sample was then centrifuged, and the acetic leach discarded and the sample rinsed with Milli-Q water. Following this a further aliquot of 2% acetic acid was added to dissolve 40% of the sample carbonate and left to react for 30 minutes. The sample was then centrifuged, and the leachate collected for Sr isotope analysis.

The leachate collected was then centrifuged to remove insoluble residues and then decanted, dried, and subsequently dissolved in HNO_3. Strontium separation by cation exchange was carried out using automatic column chromatography separation device, see Zhou et al., (2021) [55] for details. Approximately 200–300 ng of the dried sample was transferred onto a degassed and pre-baked high purity Re filament with Ta_2O_5 activator. The prepared filaments were measured using the VG Sector 54 thermal ionisation mass spectrometer in the Thermal Ionisation Mass Spectrometry facility of China University of Geoscience (Wuhan). Filaments were transferred to a sample carousel, heated under vacuum to a temperature between 1450 and 1650 °C, and analysed when a stable

562 signal was detected on the mass 88 ion beam. Approximately 100 $^{87}Sr/^{86}Sr$ ratio data points were
563 collected for each sample. Final data have been corrected for fractionation using the standard value
564 $^{86}Sr/^{88}Sr = 0.1194$. The fraction of ^{87}Sr resulting from in situ decay from ^{87}Rb was removed by
565 measurement of rubidium abundance at mass 85. Repeated analysis of the BCR-2 and BHVO-2
566 standards yields an average value of $^{87}Sr/^{86}Sr = 0.70498$ and 0.70347 ± 0.00001 (2σ) during the
567 analytical window.
568
569 **Carbonate precipitation experiments**
570 The precipitation of carbonate and uptake of CAP from seawater solutions followed previous
571 methodologies [29]. In brief, a peristaltic pump was used to add solutions of 1M $CaCl_2$ and 1M Na_2CO_3
572 with KH_2PO_4 to 1L solutions of synthetic seawater made to emulate modern day seawater chemistry.
573 Solutions were constantly stirred, and an air pump was used to bubble air through the solution in
574 order to maintain a stable pH. For precipitation rate experiments variable amounts of carbonate
575 seeds were used to vary the precipitation rate in conjunction with varying the pump rates of $CaCl_2$
576 and Na_2CO_3. Solution chemistry was checked periodically for pH, alkalinity, calcium and phosphorus
577 concentrations. A Thermofisher pH electrode was used to check pH with an accuracy better than $\pm$
578 0.1 units, alkalinity was measured by titration of seawater aliquots with 0.1M HCl, phosphorus and
579 calcium were measured as outlined above in CAP analysis. At the end of the experimental run,
580 carbonate was collected by filtration through 0.2 μm PES filters and the carbonate washed with 1M
581 $NaHCO_3$ until phosphorus concentrations in the washes were below detection. Once the carbonate
582 samples were clean of adsorbed phosphorus, 0.1g was completely dissolved in 2M HCl and

583 solutions subsequently analysed for P, Ca, and Mg as outlined above in CAP analysis. Carbonate
584 precipitation rates were calculated as mole/m^2/s following Barkan et al. (2020) [54].
585
586 **COPSE biogeochemical modelling**
587 The COPSE model was used to calculate biogeochemical feedbacks between P cycle and DOM
588 oxidation during the Shuram Excursion (SE). This model follows the work of ref. [55] and is solved in
589 MATLAB using the Ordinary Differential Equation (ODE) suite. Here, we provide a key description
590 of our model work, and the full description of our model work is given in the Supplementary
591 Information.
592 **Steady-state calculation for low background phosphorus concentration under high ocean**
593 **anoxia in Ediacaran oceans.** Based on the observed CAP and redox proxy trends across the SE
594 we can infer that a mechanism(s) was maintaining P at lower levels during the early Stage I and
595 Stage IV of the SE under high ocean anoxia. While it is ambiguous what mechanism(s) could
596 maintain a lower P reservoir under anoxia during the Ediacaran [4-6,15], we chose to modify the iron-
597 bound P burial (Equation 1) to maintain a low oceanic P reservoir during high ocean anoxia because
598 Fe^{2+}-P burial is being recently recognized as an important P sink in Precambrian ferruginous-
599 dominated oceans (see Supplementary Information 6 for rationale) [11, 14-16], but also allow for an
600 increase in oceanic P burial with decreasing ocean anoxia as modern P cycle. We stress that this
601 modification of the COPSE model is a qualitative change, as there are no current quantitative
602 relationships for Fe^{2+}-P burial. Importantly, this modification does not significantly change the model
603 results between model runs with and without Fe^{2+}-P burial; except for lowering ocean P levels under
604 high ocean anoxia (Extended Data Fig. 7). Therefore, this modification is appropriate for this study,

however future modelling work will require field relationships linking enhanced P burial under anoxia to produce more meaningful results. Thus, we modified the flux of iron-bound P burial in the standard COPSE model and include a ferrous iron scavenging flux that has a positive relationship with the degree of anoxia (ANOX) as below:

$$\mathrm{fepb}_{sws} = \frac{k_1}{k_2} \cdot \frac{P_t}{P_0} \quad (1)$$

$$\mathrm{fepb}_{fe3} = \mathrm{fepb}_{sws} \cdot (1 - ANOX) = \frac{k_1}{k_2} \cdot \frac{P_t}{P_0} \cdot (1 - ANOX) \quad (2)$$

$$\mathrm{fepb}_{fe2} = \left(\mathrm{fepb}_{sws} - \mathrm{fepb}_{fe3}\right) \cdot ANOX = \frac{k_1}{k_2} \cdot \frac{P_t}{P_0} \cdot ANOX^2 \quad (3)$$

$$\mathrm{fepb}_{tot} = \mathrm{fepb}_{fe3} + \mathrm{fepb}_{fe2} = \frac{k_1}{k_2} \cdot \frac{P_t}{P_0} \cdot (ANOX^2 - ANOX + 1) \quad (4)$$

Here fepb_{sws} is the flux of iron-bound P burial reaching the seawater-sediment interface, and fepb_{fe3} is the final flux of P that is buried with Fe^{3+}, while fepb_{fe2} is the Fe^{2+} scavenging flux including vivianite burial, and fepb_{tot} is the total flux of iron-bound P burial. P_t and P_0 are the mass of the marine P reservoir at time t and present day, respectively. $k_1 = 10^9\ \mathrm{mol\ P\ yr^{-1}}$ and $k_2 = 0.997527$ are constants, and $0 < ANOX < 0.997527$. This modification changes the original definition of the total iron-bound P burial which is negatively correlated with anoxia in the standard COPSE model. In practice, this allows for a low ocean P concentration in anoxic-ferruginous Precambrian oceans given a pO_2 = 0.01 PAL (see Supplementary Information for details of Fe-scavenging). We chose this modelling approach because the simplistic separation of Fe-P burial into Fe^{2+}- and Fe^{3+}-P burial allowed us to increase P burial under high ANOX (per the CAP and redox data) while also keeping the original COPSE model P and O_2 cycle in effect.

Weathering sulphate input. We run the COPSE model to steady state, forcing the model conditions to represent the expected geochemical conditions for Ediacaran period. We included a DOM

reservoir that responds to a weathering sulphate pulse ($sulfate_{pulse}$), which uses a simple step-forcing that follows previous work [37]. The time-dependent forcing function for the sulphate pulse is:

$$sulfate_{pulse} = interp1([-10\ 0\ 1\ 15\ 16\ 30], [0\ 0\ x\ x\ 0\ 0])$$

where the first vector is time (m.y.) and the second vector is the additional sulphate input relative to the background weathering flux (x = 3, 4, or 5). The sulphate pulse is set to last for ~15 million years, which follows the geological $^{87}Sr/^{86}Sr$ and εNd(t) records for elevated weathering input during the SE [43], as well as the rough time-taken for the duration of the SE (see Supplementary Information 5 for details on the age framework of the SE). For the model runs in the manuscript, both normal steady-state 'background' flux (subscript 'background') and additional weathering pulse input (subscript 'pulse') are working together and respond to changing geochemical conditions:

$$gypw_{background} = k_{gypw} \cdot U \cdot R \cdot \frac{carbw}{k_{carbw}} \quad (5)$$

$$gypw_{pulse} = gypw_{background} \cdot sulfate_{pulse} \quad (6)$$

$$pyrw_{background} = k_{pyrw} \cdot U \cdot R \cdot \frac{carbw}{k_{carbw}} \quad (7)$$

$$pyrw_{pulse} = pyrw_{background} \cdot sulfate_{pulse} \quad (8)$$

Here the k_{gypw} and k_{pyrw} are the present-day weathering rates of gypsum and pyrite, U and R are the normalised uplift and river runoff forcing, and the $\frac{carbw}{k_{carbw}}$ is a climate dependence representing the effect of pCO_2 on global carbonate weathering. For this study, the test case of x = 5 is used for our idealised ('best fit') scenario (Extended Data Fig. 6), which maintains a negative $\delta^{13}C_{carb}$ excursion of ca. –10 ‰ for million years.

DOM oxidation. The size of the DOM reservoir (model term DOC) is set at the beginning of the model run. This reservoir has an output flux via DOM oxidation, which is driven by sulphate reduction

[37]:

$$\frac{dDOC}{dt} = \begin{cases} 0, & DOC < 10^{12}\ mol \\ 2 \cdot \left(gypw_{pulse} + pyrw_{pulse}\right) \cdot \frac{S_t}{S_0} \cdot \frac{DOC_t}{DOC_0}, & DOC \geq 10^{12}\ mol \end{cases} \quad (9)$$

Here S_t and S_0 are the mass of the marine sulphate reservoirs at time t and present day, DOC_t and DOC_0 are the mass of DOM reservoir at t time and pre-SE, respectively. The $DOC_0 = 30$ times the mass of the modern DIC reservoir following previous estimation, in order to maintain a $\delta^{13}C_{carb}$ excursion of ~15 million years and reaching values of –10 ‰. We consider sulphate as the only direct oxidant for DOM oxidation, and its additional pulses set the rate of DOM consumption. The normal background sulphate fluxes are set not to be involved in DOM oxidation, but instead balance the oxidation of fresh organic carbon. In nature, free oxygen can also oxidise DOM once its local concentration crosses over a certain threshold (e.g., ~4 μM[58]. We also test this possibility of DOM oxidation by free oxygen using two output fluxes via both sulphate and oxygen, which is given in the Extended Data Fig. 3 and Supplementary Information 7. We follow previous models that set DOM oxidation to terminate when the DOM reservoir becomes smaller than 10^{12} moles, rather than zero, to prevent system instability [37].

Sulphate burial. The COPSE model assumes that marine sulphate is removed via the burial of gypsum and pyrite, which are linearly proportional to the total oceanic sulphate concentration [55]. In order to balance the additional sulphate input, we add additional fluxes of both gypsum ($mgsb_{additional}$) and pyrite ($mpsb_{additional}$) burial, among which the pyrite burial is equal to half the DOM oxidation rate. The remaining sulphate pulse that is not consumed by DOM is assumed to be buried as gypsum:

$$mgsb_{additional} = \left(gypw_{pulse} + pyrw_{pulse} - \frac{dDOC}{2 \cdot dt}\right) \cdot \frac{S_t}{S_0} \quad (10)$$

$$mpsb_{additional} = \frac{dDOC}{2 \cdot dt} \quad (11)$$

Phosphorus mass balance. In this study, elevated sulphate supply to the Ediacaran Ocean, following previous proposals [24], is proposed to create a large long-term oxidant source. This input of oxidising power oxidised a large marine DOM pool, releasing DIC and P. The P released by DOM oxidation ($pdoc$) is assumed to be a net source for the marine P reservoir, which is calculated using the rate of DOM oxidation ($\frac{dDOC}{dt}$) and the C/P_{DOC} ratio. The new P mass is estimated with the following equations, adapted from ref. [55]:

$$\frac{dP}{dt} = psea + pdoc - mopb - capb - fepb_{tot} \quad (12)$$

Here $psea$ is the weathering flux of reactive P to the ocean, $mopb$ and $capb$ is P burial with organic carbon and calcium, respectively. We chose a fixed ratio of $C/P_{DOC} = 1000$ as the default, but also tested the influence of changing C/P_{DOC} (250, 1000, 3500, and no P release) on the marine P concentration (see Extend Data Fig. 4).

Full model description. See Supplementary Information for full modified COPSE model equations and parameters.

Code availability.

MATLAB code for COPSE is freely available at https://github.com/sjdaines/COPSE/releases.

Methods References

51 Cui, H. *et al.* Redox architecture of an Ediacaran ocean margin: Integrated chemostratigraphic (δ13C–δ34S–87Sr/86Sr–Ce/Ce*) correlation of the Doushantuo Formation, South China. *Chemical Geology* **405**, 48-62, doi:https://doi.org/10.1016/j.chemgeo.2015.04.009 (2015).

52 Bellefroid, E. J., Planavsky, N. J., Miller, N. R., Brand, U. & Wang, C. Case studies on the utility of sequential carbonate leaching for radiogenic strontium isotope analysis. *Chemical Geology* **497**, 88-99, doi:https://doi.org/10.1016/j.chemgeo.2018.08.025 (2018).

53 Zhou, F.-Y. *et al.* Development of an Automatic Column Chromatography Separation Device for Metal Isotope Analysis Based on Droplet Counting. *Analytical Chemistry* **93**, 7196-7203, doi:10.1021/acs.analchem.1c00145 (2021).
54 Barkan, Y., Paris, G., Webb, S. M., Adkins, J. F. & Halevy, I. Sulfur isotope fractionation between aqueous and carbonate-associated sulfate in abiotic calcite and aragonite. *Geochimica et Cosmochimica Acta* **280**, 317-339, doi:https://doi.org/10.1016/j.gca.2020.03.022 (2020).
55 Lenton, T. M., Daines, S. J. & Mills, B. J. W. COPSE reloaded: An improved model of biogeochemical cycling over Phanerozoic time. *Earth-Science Reviews* **178**, 1-28, doi:10.1016/j.earscirev.2017.12.004 (2018).

Main text figure captions

Figure 1. Carbonate-Associated Phosphate (CAP; given as CAP/(Ca+Mg)) and accompanying key geochemical records in six globally distributed sections which recorded the Shuram Excursion (SE), the largest known negative C-isotope excursion in carbonate ($\delta^{13}C_{carb}$) from the geological record. a) Global palaeogeographic map showing the locations of study regions (red stars) at ~560 Ma, modified after ref. [25]. b) Jiulongwan section (South China); c) Cerro Rajón section (Mexico), inset graph shows entire Ediacaran section; d) Death Valley section (USA), e) Parachilna Gorge section (Australia). f) Mochia-Khutuk section (North-western China), g) Sishang section (South China). Geochemical data sources: CAP and $^{87}Sr/^{86}Sr$ data are from this study, also $\delta^{13}C_{carb}$ of the Sishang and Parachilna Gorge sections are data from this study; other C-, U- and S-isotope data from refs.[7,8,21,22,23,24,26,27]. P-1st = first CAP peak; P-2nd = second CAP peak. PQ Fm., Pitiquito Formation; Gm Fm., Gamuza Formation; DY Fm., Dengying Formation; VPDB, Vienna Pee Dee Belemnite; VCDT, Vienna Canyon Diablo Troilite. Stratigraphic heights are meters above the first exposed outcrops of Ediacaran strata, except in the Death Valley, Parachilna and Mochia-Khutuk sections which are meters above the lower boundary of the measured geological formation and Sishang metres below Dengying Formation. Light blue circles are CAP in calcite and dark blue circles CAP in dolomite. White circles are $\delta^{13}C_{carb}$ and CAP outliers and error bars show a 5% error

margin. Black line through CAP data = LOESS smoothing. Stages I to IV are defined as follows: Stage I (falling limb of $\delta^{13}C_{carb}$), Stage II (plateau of $\delta^{13}C_{carb}$ values), Stage III (rising limb of $\delta^{13}C_{carb}$) and Stage IV (return to pre-SE $\delta^{13}C_{carb}$ values). See Supplementary Information 2 for correlation between sections and published data.

Figure 2. Conceptual model illustrating the co-evolution of the phosphorus cycle and dissolved organic matter (DOM) oxidation during the Shuram Excursion (SE) (see text for detailed description of the panels). a) Increasing weathering sulphate oxidises oceanic DOM increasing oceanic P and atmospheric O_2 and CO_2; b) elevated atmospheric O_2 decreases ocean anoxia and increases sedimentary P burial; c) cessation of DOM oxidation and pyrite burial leads to a decrease in atmospheric O_2 and the return of ocean anoxia. Stage I-IV refers to SE stages I-IV in Figure 1. Arrows from Fe^{2+} and Fe^{3+} signify the burial of P with Fe under anoxic and oxic conditions, respectively.

Figure 3. Biogeochemical model results which best replicate the observed Carbonate-Associated Phosphate (CAP) and C- and U-isotope records in Figure 1. a) Ocean carbonate C-isotopic composition ($\delta^{13}C_{carb}$); b) ocean P concentration ($[P]_{sw}$); c) ocean carbonate uranium isotopic composition ($\delta^{238}U_{carb}$); d) ocean sulphate sulphur isotopic composition ($\delta^{34}S_{CAS}$); e) ocean carbonate strontium isotopic composition ($^{87}Sr/^{86}Sr$); f) Ediacaran fossil record (adopted after ref [19]). Note the different time axes of panels a-e from panel f. Stage I-IV and P-1st and P-2nd refer to Shuram Excursion (SE) $\delta^{13}C_{carb}$ profile and CAP peaks in Figure 1, respectively. Turquoise lines represent model run with continuous Fe^{2+}-P burial and no HCO_3^- release from DOM oxidation; blue

747 lines represent Fe^{2+}-P burial stops during SE and no HCO_3^- release from DOM oxidation; dark blue
748 lines represent Fe^{2+}-P burial stops during SE and HCO_3^- released during DOM oxidation, which
749 halves CO_2 release from DOM (see Supplementary Information 4 and 6 for details).
750
751 **Extended Data Table and Figure Captions**
752
753 **Extended Data Table 1. Statistics for Carbonate-Associated Phosphate (CAP) extraction and**
754 **diagenetic measures.** The strong, statistically significant correlation between bulk rock La and bulk
755 rock P in the Jiulongwan section derives from the dissolution of phosphate minerals. Yet, no statically
756 significant correlations are seen between La and CAP in the partial leach, implying minimal
757 contamination from phosphate minerals for bulk rock P. Unless otherwise stated all elemental data
758 is derived from CAP partial leach extraction. Isotopic data is obtained for the bulk rock. Note, when
759 removing < 10% of data points as outliers, significant levels [P(α)] all increase above 0.01 for all
760 sections, indicating statistically insignificant correlations. All trendlines are linear fits. TOC = Total
761 Organic Carbon.
762
763 **Extended Data Figure 1. Open system diagenetic evolution fluid-rock interaction model.** (a-c)
764 Fluid -rock alteration models showing the relative order of alteration for CAP, CAS, Fe, Mn, IO_3, $\delta^{13}C$,
765 $\delta^{34}S_{CAS}$, $\delta^{238}U$, $\delta^{44/40}Ca$, $^{87}Sr/^{86}Sr$. Multiple curves are presented for $\delta^{13}C$ and $\delta^{34}S_{CAS}$ under varying
766 dissolved inorganic carbon (DIC) and sulphate concentrations in the diagenetic fluid. (d) Fluid-rock
767 alteration model showing the predicted trends between CAP and $\delta^{13}C$, grey points are CAP and
768 $\delta^{13}C$ data from all study sections. Solid and dashed lines represent different pore water DIC

769 concentration and $\delta^{13}C$ compositions. Dotted line is trendline through datapoints with R value. See
770 Supplementary Information for model description. Yellow stars mark the point at which 50% of the
771 CAP value has been altered, the red/ grey stars mark the point at which 50% of the element of
772 interest has been altered. CAP = Carbonate-Associated Phosphate, CAS = Carbonate-Associated
773 Sulphate.
774
775 **Extended Data Figure 2. COPSE model results comparing different hypotheses (dissolved**
776 **organic matter (DOM) oxidation by sulphate only, elevated organic matter recycling, elevated**
777 **weathering by uplift, elevated weathering by volcanism) for the observed changes in ocean**
778 **P during the Shuram Excursion. a, A, I, i**. Relative increase in sulphate addition versus
779 background flux. **b, B, II, ii**. Phosphorus concentration in seawater ($[P]_{sw}$). **c, C, III, iii**. Relative
780 atmospheric oxygen concentration (pO_2). **d, D, IV, iv**. Degree of ocean anoxia (Anoxia). **e, E, V, v**.
781 Modelled marine carbonate carbon isotope composition ($\delta^{13}C_{carb}$). Note in panel E, the $\delta^{13}C_{carb}$
782 reflects the $\delta^{13}C$ of porewater dissolved inorganic carbon (DIC), not oceanic $\delta^{13}C$. **f, F, VI, vi**.
783 Modelled marine sulphate sulphur isotope composition ($\delta^{34}S_{sulphate}$). **g, G, VII, vii**. Modelled marine
784 carbonate uranium isotope composition ($\delta^{238}U_{carb}$). For the DOM oxidation hypothesis, we run the
785 COPSE model with a DOM reservoir 30 times the size of the modern marine DIC reservoir and the
786 C:P of the DOM reservoir is 1000, while the C:P of organic matter in the organic matter recycle
787 model is 250 (see Supplementary Information 6 for more details). PAL = Present Atmospheric Level.
788
789 **Extended Data Figure 3. COPSE model results comparing the oxidation of a dissolve organic**
790 **matter (DOM) reservoir using sulphate, free oxygen (Shields et al., 2019) and sulphate + free**

oxygen, respectively. a, A, I Relative increase in sulphate addition versus background flux (the varying colour shades of the model lines reflect the varying magnitude of the sulphate pulse for different model runs). **b, B, II**. Phosphorus concentration in seawater ($[P]_{sw}$). **c, C, III**. Relative atmospheric oxygen concentration (pO_2). **d, D, IV**. Degree of ocean anoxia (Anoxia). **e, E, V**. Modelled marine carbonate carbon isotope composition ($\delta^{13}C_{carb}$). **f, F, VI**. Modelled marine sulphate sulphur isotope composition ($\delta^{34}S_{sulphate}$). The C:P of the DOM reservoir is set to 1000 in all model runs. The magnitude of the sulphate pulses for each model is variable because higher additional sulphate fluxes are required for models where DOM is oxidised by O_2 resulting from pyrite burial, in comparison to models where DOM is oxidised only by sulphate (see Supplementary Information 7 for details).

Extended Data Figure 4. COPSE model results with varying sizes (sub-figures A-F) and variable P content (a-d) of an initial dissolved organic matter (DOM) reservoir and higher initial steady-state pO_2 of 20% present atmospheric level (PAL), with C:P of DOM = 250 (sub-figures a-d) (no Fe^{2+}-P burial) (sub-figures I-IV). A. Size of DOM reservoir in moles of carbon. **B**. Phosphorus concentration in seawater ($[P]_{sw}$). **C**. Relative atmospheric oxygen concentration (pO_2). **D**. Degree of ocean anoxia (Anoxia). **E**. Modelled marine carbonate carbon isotope composition ($\delta^{13}C_{carb}$). **F**. Modelled marine carbonate uranium isotope composition ($\delta^{238}U_{carb}$).. In panels A-F, we choose an additional sulphate pulse of 4 times that of the background flux and the C:P of the DOM reservoir is 1000. **a, I**. Size of DOM reservoir in moles of carbon. **b, II**. Phosphorus concentration in seawater ($[P]_{sw}$). **c, III**. Relative atmospheric oxygen concentration (pO_2). **d, IV**. Degree of ocean anoxia. In panels a-d, we choose a sulphate input of 4 times the background flux and the size of the

DOM reservoir is 30 times that of the size of the modern marine dissolved inorganic carbon (DIC) reservoir. For panels I-IV, the DOM reservoir is 30 times that of the size of the modern marine dissolved inorganic carbon (DIC). Higher steady-state pO_2 was achieved by adjusting the model terrestrial P input flux and gypsum burial.

Extended Data Figure 5. COPSE model results varying the magnitude of an additional sulphate pulse for dissolved organic matter (DOM) oxidation by sulphate only (no Fe^{2+}-P burial) (a-h), burying all additional sulphate pulse as pyrite (I-VIII) and setting gypsum burial to a constant rate (i-viii). a. Size of DOM reservoir in moles of carbon. **b**. Modelled marine carbonate carbon isotope composition ($\delta^{13}C_{carb}$). **c**. Phosphorus concentration in seawater ($[P]_{sw}$). **d**. Modelled marine carbonate uranium isotope composition ($\delta^{238}U_{carb}$). **e**. Relative atmospheric oxygen concentration (pO_2). **f**. Degree of ocean anoxia. **g**. Modelled marine sulphate sulphur isotope composition ($\delta^{34}S_{sulphate}$). **h**. Modelled marine carbonate strontium isotope composition ($^{87}Sr/\ ^{86}Sr$). The blue line, the grey line, and the dashed grey line are additional sulphate pulses of 3, 4 and 5 times the background flux respectively. **I, i.** Relative atmospheric oxygen concentration (pO_2). **II, ii.** Phosphorus concentration in seawater ($[P]_{sw}$). **III, iii.** Modelled marine carbonate carbon isotope composition ($\delta^{13}C_{carb}$). **VI, vi.** evolution of ocean anoxia. **V, v.** Modelled marine carbonate uranium isotope composition ($\delta^{238}U_{carb}$). **VI, vi.** Modelled marine sulphate sulphur isotope composition ($\delta^{34}S_{sulphate}$). **VII, vii.** Sulphate concentration in seawater ($[SO_4]_{sw}$). **VIII, viii.** Oceanic gypsum burial rate (mgsb). Here we used a DOM reservoir size that is 30 times that of the size of the modern marine dissolved inorganic carbon (DIC) reservoir. PAL = present atmospheric level, POL = present oceanic level.

335

336 **Extended Data Figure 6. Full COPSE model outputs for dissolved organic matter (DOM)**
337 **oxidation by sulphate with constant (Fe^{2+}) -bound phosphorus burial, using a sulphate pulse**
338 **of 4 times background flux, DOM C:P of 1000, and the size of the DOM reservoir is 30 times**
339 **the size of the modern marine dissolved inorganic carbon (DIC) reservoir. a.** Weathering
340 sulphate pulse versus background flux. **b.** DOM oxidation flux (DOM_{ox}) in moles of carbon per year.
341 **c.** DOM reservoir (DOM_{pool}) in moles of carbon. **d.** P concentration in sea water ($[P]_{sw}$). **e.** Relative
342 atmospheric oxygen concentration (pO_2) to present atmospheric level (PAL). **f.** Degree of marine
343 anoxia (Anoxia). **g.** Modelled marine carbonate carbon isotope composition ($\delta^{13}C_{carb}$). **h.** Modelled
344 marine sulphate sulphur isotope composition ($\delta^{34}S_{sulphate}$). **i.** Silicate weathering flux (silw) in moles
345 of carbon per year. **j.** Modelled marine carbonate strontium isotope composition ($^{87}Sr/\ ^{86}Sr$). **k.**
346 Relative marine sulphate concentration ($[SO_4^{2-}]_{sw}$) to present oceanic level (POL). **l.** Relative marine
347 new primary productivity (newp) to POL. **m.** Relative atmospheric carbon dioxide concentration
348 (pCO_2) to PAL. **n.** Average global temperature (Temp) in ℃. **o.** Organic carbon weathering flux
349 (oxidw) in moles of carbon per year. **p.** Marine organic carbon burial flux (mocb) in moles of carbon.
350 **q.** Gypsum sulfur weathering flux (gypw) in moles of sulfur. **r.** Pyrite sulfur weathering flux (pyrw) in
351 moles of sulfur. **s.** Marine pyrite sulphur burial flux (mpsb) in moles of sulphur. **t.** Marine gypsum
352 sulphur burial flux (mgsb) in moles of sulphur. **u.** Phosphorus releasing flux from DOM oxidation
353 (DOM_{OX}_P) in moles of phosphorus. **v.** Flux of weathered phosphorus reaching the sea (psea) in
354 moles of phosphorus. **w.** Total iron-bound phosphorus burial flux (fepb) in moles of phosphorus. **x.**
355 Carbonate-bound phosphorus burial flux (capb) in moles of phosphorus. **y.** Marine organic
356 phosphorus burial flux (mopb) in moles of phosphorus. **z.** Ferric iron (Fe^{3+}) -bound phosphorus burial

357 [fepb(Fe^{3+})] in moles of phosphorus. **aa.** Ferrous iron (Fe^{2+}) -bound phosphorus burial [fepb(Fe^{2+})]
358 in moles of phosphorus.
359
360 **Extended Data Figure 7. Comparison of COPSE model results for ocean P cycling with and**
361 **without P burial by Fe^{2+} scavenging. a.** Ocean inorganic carbon isotopic composition ($\delta^{13}C_{carb}$). **b.**
362 Ocean P concentration ($[P]_{sw}$); red shaded areas represent uncertainty windows in Fig. 3. **c.** Ocean
363 uranium isotopic composition recorded in carbonates ($\delta^{238}U_{carb}$). **d.** Ocean sulphur isotopic
364 composition recorded in carbonate-associated sulphate ($\delta^{34}S_{CAS}$). **e.** Ocean strontium isotopic
365 composition ($^{87}Sr/^{86}Sr$). **f.** Ediacaran fossil record adapted after Darroch et al. (2018). Stages I to IV
366 are defined as the SE intervals of falling limb, plateau, rising limb and post-SE, respectively, as in
367 Figure 1 which are matched with modelled ocean P reservoir shifts. Model parameters for outputs
368 are the same as detailed in Fig. 3 and Extended Data Fig. 6 except for the red line which excludes
369 P burial by Fe^{2+}-scavenging (i.e., a modern-style P and O_2 cycle). P-1^{st} and P-2^{nd} refers to carbonate-
370 associated phosphate (CAP) peaks in Figure 1.
371
372 **Extended Data Figure 8. Model output of a quantitative 4-box ocean P cycle model.** Output
373 from Figures 4a and 5a in Alcott et al. (2019) with the P concentrations in the respective boxes
374 (proximal shelf, distal shelf, deep ocean) plotted. This shows the relative concentration of soluble
375 reactive phosphorus in each ocean box during a model solution in which P levels are oscillating on
376 a large scale. These results show that even under substantial changes in P concentration, the distal
377 shelf (i.e., the area of the shelf that is not dominated by riverine input) is expected to be strongly
378 linked to the deep ocean P concentration. See Alcott et al. (2019) for full model details.

Extended data Figure 9. Experimental constraints on the effects of alkalinity (a) and precipitation rate (b) on carbonate-associated phosphate (CAP) values in carbonate. a. CAP uptake increases with progressively lower [CO_3^{2-}] and alkalinity concentrations. **b.** CAP uptake decreases with increasing precipitation rate. The changes in CAP over the observed ranges in alkalinity and precipitation rate are small compared to the effects of phosphate concentration and solution pH (Dodd et al., 2021). All trendlines are linear fits. Error bars are ± 5% for CAP and ± 0.1 for Ca/ ALK.

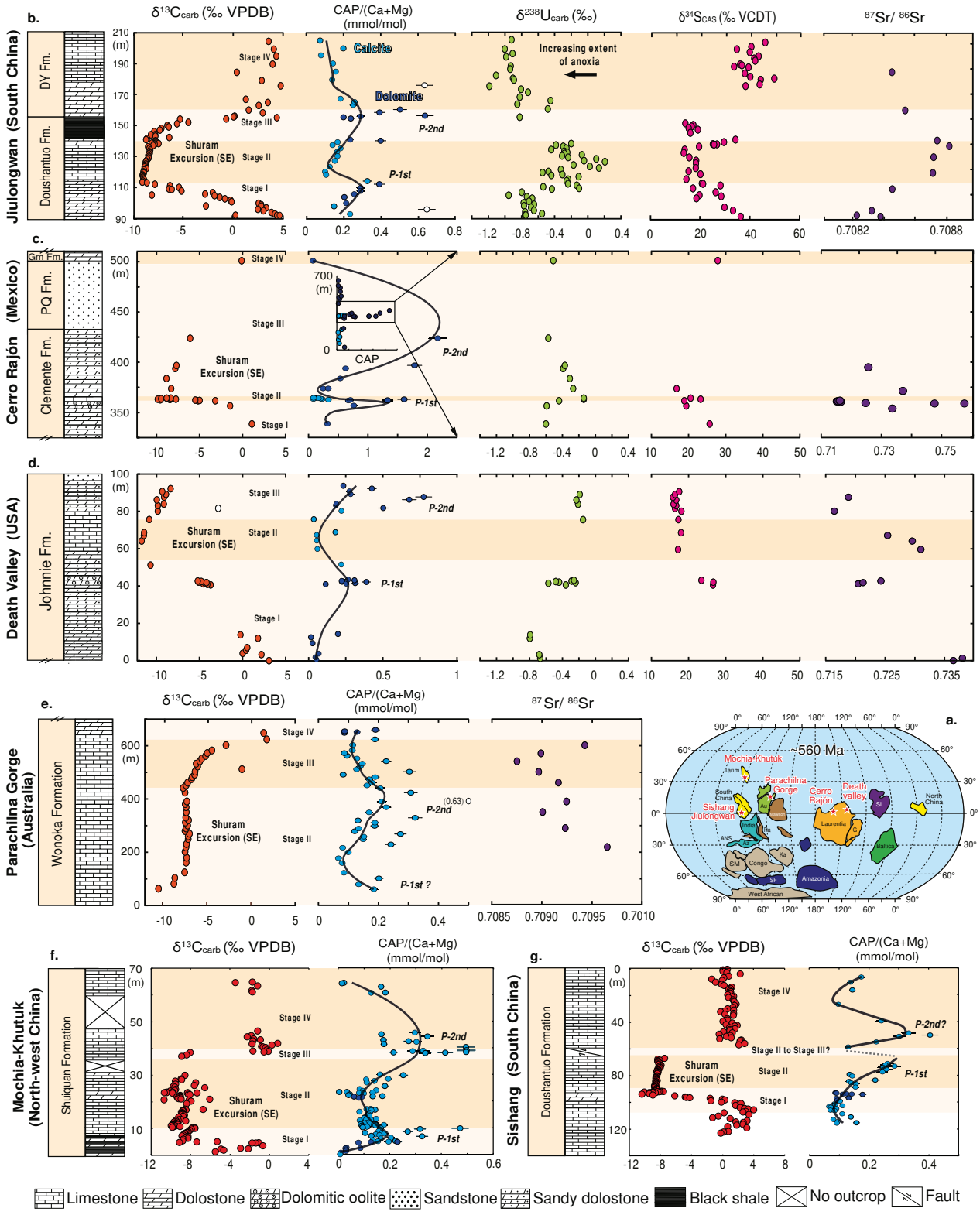
b.
Jiulongwan (South China)
DY Fm.
Doushantuo Fm.
δ13Ccarb (‰ VPDB)
CAP/(Ca+Mg) (mmol/mol)
δ238Ucarb (‰)
δ34SCAS (‰ VCDT)
87Sr/ 86Sr
Calcite
Dolomite
Increasing extent of anoxia
Stage IV
Stage III
Stage II
Stage I
Shuram Excursion (SE)
P-2nd
P-1st
c.
Cerro Rajón (Mexico)
Gm Fm.
PQ Fm.
Clemente Fm.
CAP
d.
Death Valley (USA)
Johnnie Fm.
e.
Parachilna Gorge (Australia)
Wonoka Formation
P-1st ?
a.
~560 Ma
Mochia-Khutuk
Parachilna Gorge
Cerro Rajón
Death valley
Sishang
Jiulongwan
f.
Mochia-Khutuk (North-west China)
Shuiquan Formation
g.
Sishang (South China)
Doushantuo Formation
Stage II to Stage III?
P-2nd?
Limestone
Dolostone
Dolomitic oolite
Sandstone
Sandy dolostone
Black shale
No outcrop
Fault

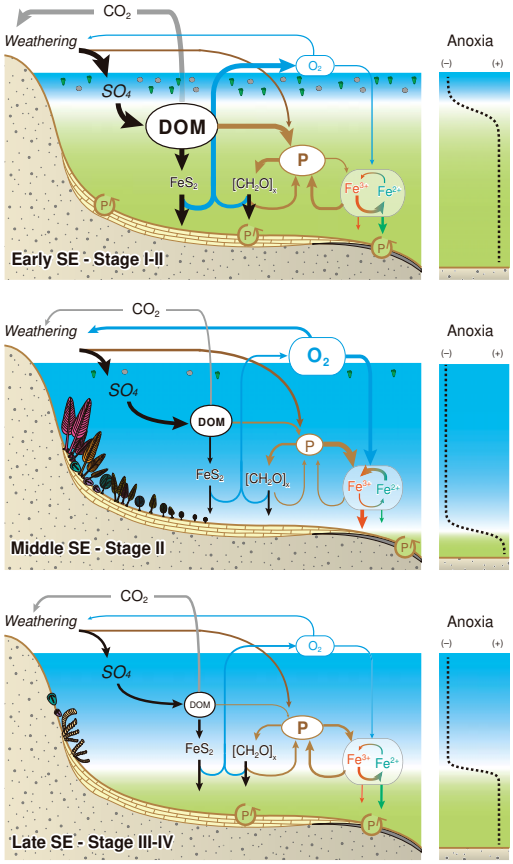
CO2
Weathering
O2
SO4
DOM
P
FeS2
[CH2O]x
Fe3+
Fe2+
Anoxia
(–)
(+)
Early SE - Stage I-II
CO2
Weathering
O2
SO4
DOM
P
FeS2
[CH2O]x
Fe3+
Fe2+
Anoxia
(–)
(+)
Middle SE - Stage II
CO2
Weathering
O2
SO4
DOM
P
FeS2
[CH2O]x
Fe3+
Fe2+
Anoxia
(–)
(+)
Late SE - Stage III-IV

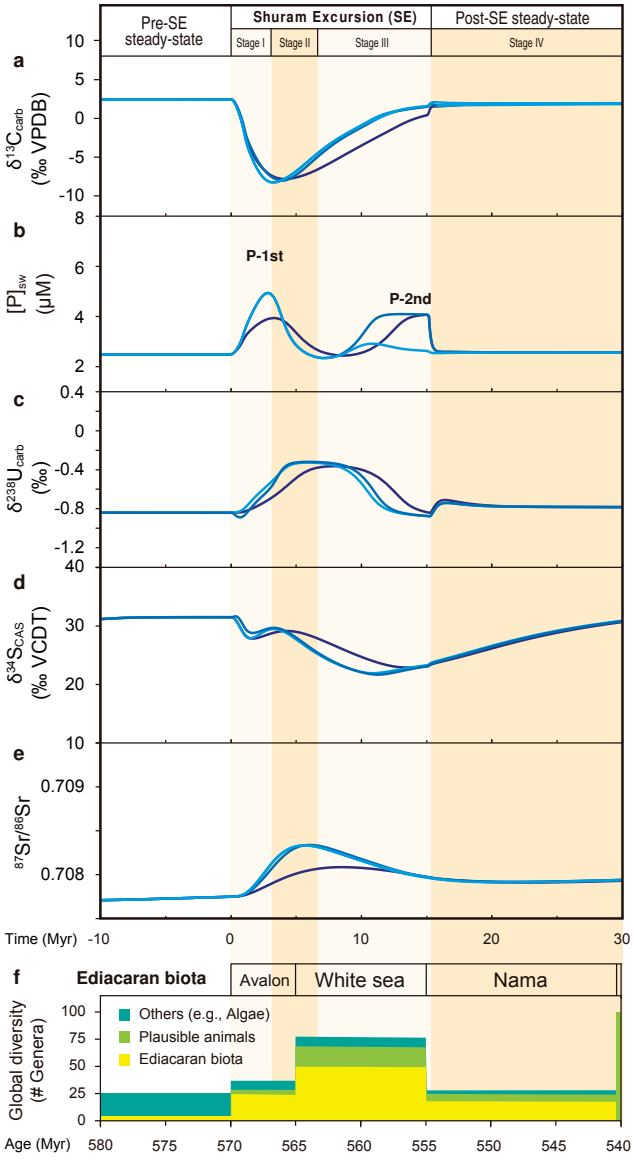
Pre-SE steady-state
Shuram Excursion (SE)
Post-SE steady-state
Stage I
Stage II
Stage III
Stage IV
a
δ13Ccarb (‰ VPDB)
b
[P]sw (μM)
P-1st
P-2nd
c
δ238Ucarb (‰)
d
δ34SCAS (‰ VCDT)
e
87Sr/86Sr
Time (Myr)
f
Ediacaran biota
Avalon
White sea
Nama
Others (e.g., Algae)
Plausible animals
Ediacaran biota
Global diversity (# Genera)
Age (Myr)